

Supporting Information for

Real Space Visualization of Entangled Excitonic States in Charged Molecular Assemblies

Jiří Doležal^{1,2*}, Sofia Canola^{1*}, Prokop Hapala¹, Rodrigo Cezar de Campos Ferreira¹, Pablo Merino^{3,4*}, Martin Švec^{1,5*}

¹Institute of Physics, Czech Academy of Sciences; Cukrovarnická 10/112, CZ16200 Praha 6, Czech Republic

²Faculty of Mathematics and Physics, Charles University; Ke Karlovu 3, CZ12116 Praha 2, Czech Republic

³Instituto de Ciencia de Materiales de Madrid; CSIC, Sor Juana Inés de la Cruz 3, E28049 Madrid, Spain

⁴Instituto de Física Fundamental, CSIC; Serrano 121, E28006 Madrid, Spain

⁵Regional Centre of Advanced Technologies and Materials; Šlechtitelů 27, CZ78371 Olomouc, Czech Republic

Simulation of the photon maps

To compare the experimentally measured photon maps with the corresponding theoretical predictions we developed a computationally efficient and universal module within the freely available Probe-Particle package,^{S1} which calculates the interaction between the electric field of a tip-enhanced plasmon, and a molecular or aggregate exciton in the sample. Following the approach developed by Neuman *et al.*,(based on Eq.(1) in ref. S2), we evaluate the coulomb integral $g(r)$ between the transition density of the excitons ρ_S of the sample (*e.g.* the molecular cluster) and the electric field V_{TIP} of the metallic tip plasmon:

$$g(r) = \int_{r'} \rho_S(r') V_{TIP}(r - r') dr' \quad (1)$$

where r represents the relative position of the tip over the sample, corresponding to a pixel in the simulated photon map and r' is a grid coordinate.

We use the calculated function $|g(r)|^2$ directly to generate the photon maps. This represents a simplification of Eq.(1) from ref. S2 by removing its energy dependence, assuming that within the narrow energy range of molecular exciton the spectrum of the plasmon is approximately constant. This approach is sufficient to study the spatial dependence of the coupling (*i.e.* the dependence on tip position r) and for the purpose of comparison with the normalized experimental photon maps in which the background and spectral dependence is largely suppressed. In our simulation, V_{TIP} is currently approximated by damped multipole expansion:

$$V_{TIP}(r) = \sum_k C_k ((z - z_0)/|r|)^{(k-1)} (1/(|r|^2 - R^2))^{(k/2)} \quad (2)$$

where k controls the order of multipole ($k = 1$ monopole, $k = 2$ dipole, *etc.*), z_0 represents the distance of the tip (the centre of the V_{TIP} multipole) from the sample, and R denotes the finite width of the tip (*i.e.* Lorentzian decay for the dipole). In line with the approach employed in ref. S2, we approximated the tip field plasmon function V_{TIP} as an electric dipole oriented in the z -direction with $z_0 = R = 5$ Å. However, we verified that photon maps are qualitatively similar if simulated using an electric monopole or a dipole oriented along the z -axis.

The transition densities ρ_S of the aggregates were obtained directly from the quantum-chemical calculations (see below for details). Both V_{TIP} and ρ_S are sampled on a regular real-space grid with resolution ~0.2 Å before the simulation, which allows us to easily update our model in future to include *e.g.* more a realistic shape of the tip.

To calculate the convolution in Eq.(1) efficiently, we employ fast fourier transform (FFT). This makes our simulation program very efficient and general. For arbitrary spatial distribution of V_{TIP} stored on a real space grid it can simulate photon-maps in a few seconds on a standard PC.

RF-PS measurements

For the RF-PS spectroscopy on a PTCDA anion we used the methodology described in our previous work.^{S3} The transmission of the wiring was calibrated at 200 MHz using broadening

of a plasmon high-energy cutoff at 1.8 V on a clean substrate.^{S4} The time frame is 50 ns and we used 64 ps bin width. For filtering of the emission line we used a hard-coated 25 nm bandpass filter (Edmund optics) with center wavelength 925 nm. Histograms are accumulated for approximately 20 min, depending on the strength of the modulation and the resulting signal-to-noise ratio in the waves (Fig.S1). At the bias of -2.1 V (onset of the luminescence) the obtained effective lifetime of the excited anionic state is within the error of the measurement which is <70 ps in this case.

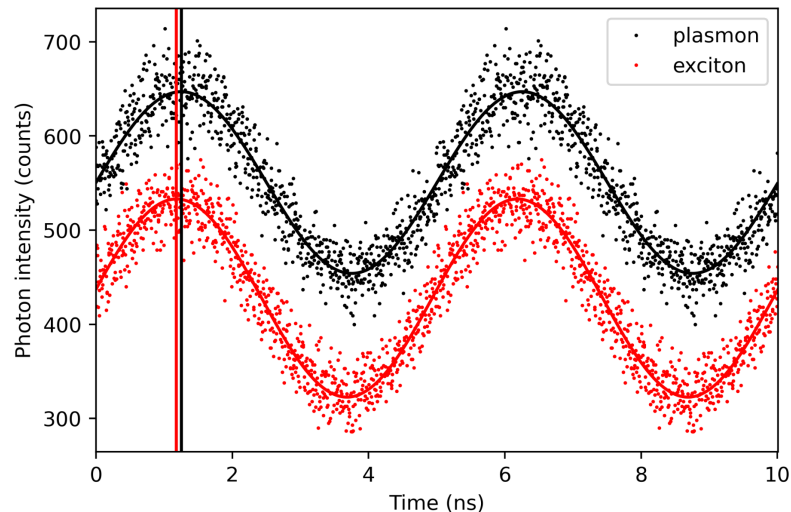


Figure S1. Radio-frequency phase-shifted waves obtained for a plasmonic reference (black) $V_{DC} = 1.5$ V, $I_t = 1$ nA, $V_{AC} = 200$ mV, integration time 1200 s on Ag(111). First excited anionic state (red) was measured with $V_{DC} = -2.1$ V, $I_t = 50$ pA, $V_{AC} = 200$ mV, integration time 1200 s at oxygen termination position on a single PTCDA on 3ML-NaCl. Sinus function with calculated phase-shift, amplitude, constant term and period as parameters is plotted with a solid line for both plasmonic reference and excited state. The difference between the reference and the excited state is marked by a vertical line.

Assembly formation on NaCl/Ag(111)

To generate the molecular assemblies of different configurations we have tested several methodologies. While molecular manipulation with the tip of the AFM/STM could be used to form molecular dimers, in order to efficiently form larger assemblies, we have adopted the thermally activated process previously described in the literature.^{S5-S7} We successfully applied this concept to the PTCDA deposited on NaCl on Ag(111) (evaporation temperature was 380°C, substrate at 10 K) and subsequently annealed for 1 min by taking the sample with a manipulator (at RT) and putting it in contact with the LN cryostat shield. With the sample cooled back below 10 K, the STM topography shows an abundance of small 2D molecular assemblies (examples at low coverage can be seen in Fig.S2). Here the driving interaction of the self-assembly stems from the attraction between the carbonyl oxygens and the hydrogen-termination along the sides of the perylene backbone of the molecules, which pushes the nearest neighbors in the clusters to perpendicular arrangements. The result of the process is sensitive to the concentration of PTCDA on the surface, annealing duration and the number

of NaCl layers on which the molecules diffuse. Higher concentrations and higher annealing times tend to produce larger islands (we have prepared clusters of up to 20 units); the largest islands tend to be formed at 3 layers of NaCl compared to 2 and 4 layer NaCl.

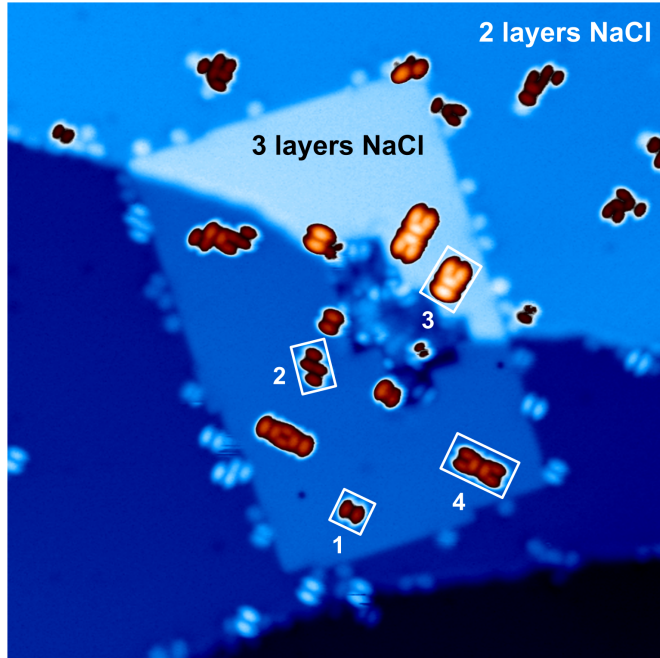


Figure S2. Example STM topography overview of the PTCDA aggregates on 2ML- and 3ML-NaCl/Au(111) system, formed by allowing diffusion of the molecules. White rectangles mark a monomer (1), two types of dimers (2,3) and a trimer (4) that were the subject of this study. The image parameters were $40 \times 40 \text{ nm}^2$, 1.2 V.

Single PTCDA on 3 layers of NaCl/Au(111) at positive bias voltage

For the lack of features and a low signal yield in the photon spectra of PTCDA at energies higher than the anion first excited state, we performed an additional measurement at positive bias voltages. Unfortunately, under these conditions the single molecule experiences instability. Nevertheless, we have discovered that on NaCl/Au(111) it remains relatively stable and therefore we were able to perform the photon spectroscopy and hyperspectral mapping at a single molecule on this surface (Fig.S3). We found the dominant contribution of the first excited anion state at 1.332 eV and a number of higher-energy peaks with large plasmonic background. In particular, the spectra taken over the H-terminated sides present a significantly larger contribution of the signal at 1.493 eV, with respect to the intensity of the first excited state. A photon map at this energy (Fig.S3c reveals a distribution of the intensity in the real space, indicative of an excited state independent of the $D_1 \rightarrow D_0$ transition. We link this feature with the decay of a second excited state (D_2), based on the comparison with the theoretical prediction (Fig.S3d,e), which associates it with a transition dipole moment perpendicular to the longitudinal plane of the molecule, resulting in a characteristic photon map with the intensity localized above the H-terminations of the molecule.

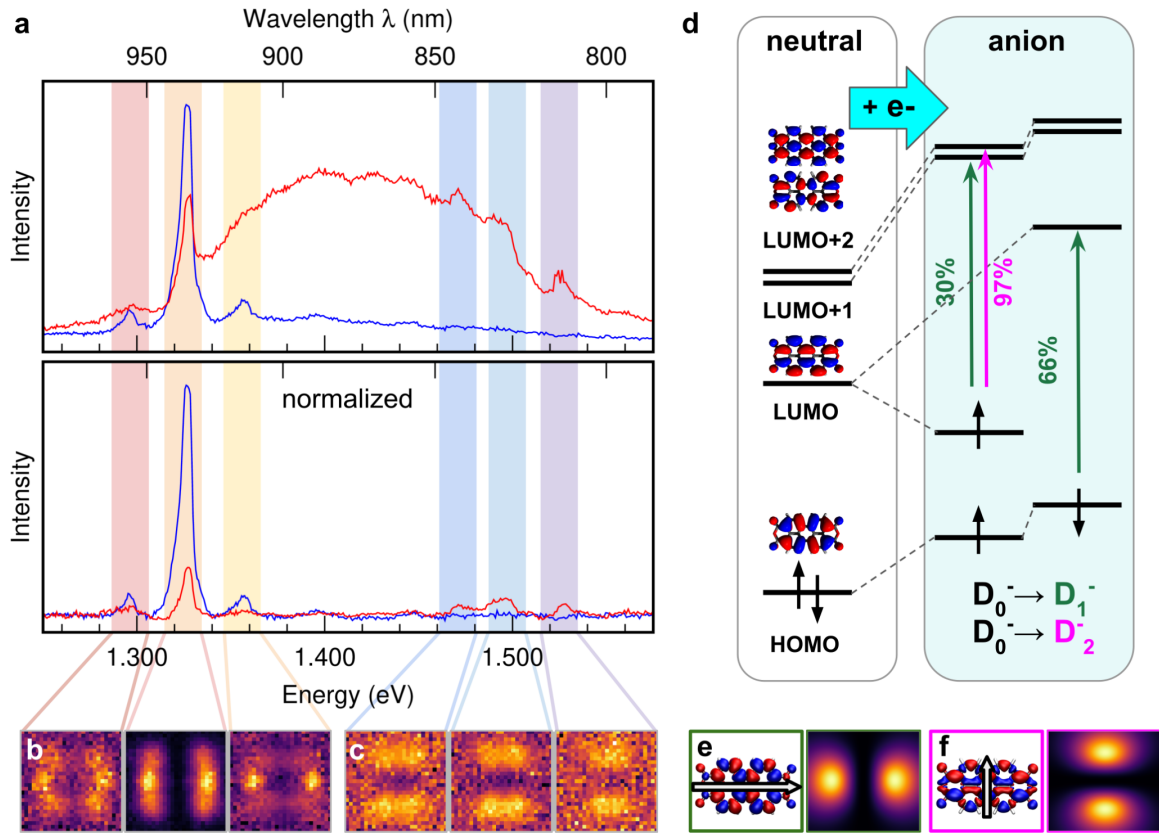


Figure S3. (a) Averaged electroluminescence spectra of PTCDA anion measured on 3ML-NaCl/Au(111), before and after (top and bottom panels, respectively) normalization by the plasmon. Measurement parameters were set to +2.5V, 100pA. (b,c) Photon maps evaluated in the spectral ranges denoted in (a). (d) Energy level schemes and corresponding orbitals obtained from calculations on the PTCDA neutral and anion states (wB97XD/6-31G*). Green and magenta arrows are marking the main transitions involved in the first two anion excited states D_1^- and D_2^- and their weight in percent. (e,f) Transition densities and their corresponding simulated photon maps of the D_1^- and D_2^- states, respectively.

Determination of the adsorption geometries with AFM

For a single PTCDA molecule, both types of dimers and the tetramer, we performed a geometrical registration with the substrate (Fig.S4). We used CO-functionalized tips to scan the molecule and the surrounding areas of NaCl substrate, each at relative tip-sample distances that yield the atomic resolution. By extrapolating the lattice of the NaCl, we determined the preferred positioning of the PTCDA, which is always on top of a Cl^- ion, with the two principal mirror planes aligned with the Cl rows.

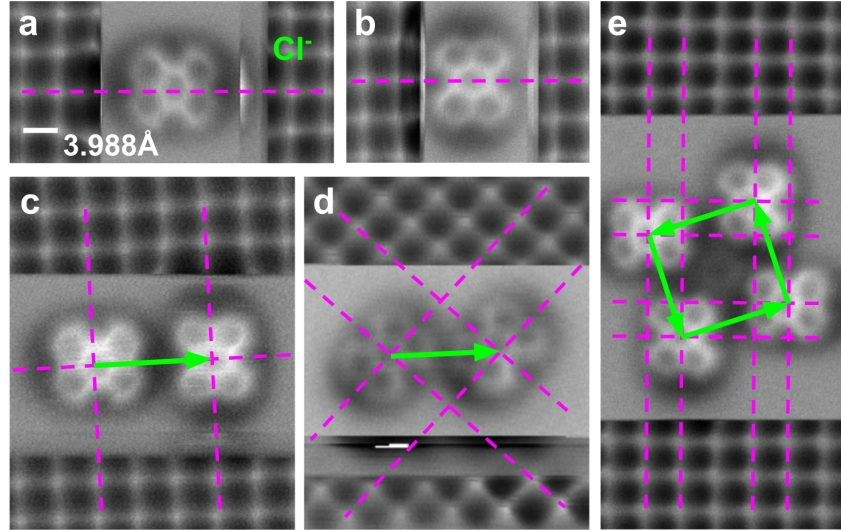


Figure S4. AFM analysis of adsorption configurations of the single PTCDA molecules (a), perpendicular dimer (b), parallel dimer (c) and tetramer (d) on NaCl(001) layers on Ag(111). Purple dashed lines mark the Cl rows which cross the centers of the PTCDA, green vectors denote the mutual displacements of the molecules in the aggregates. The bright spots in the lattice correspond to Cl^- ion locations. All images have been taken with CO-functionalized tips at bias voltage of 5mV. The absolute scale of all images can be unambiguously derived from the visible surface lattice of NaCl(001).

Normalization of the spectra and the photon maps

The individual electroluminescence spectra taken above the molecules are shaped by the spectral character of the nanocavity and the tunneling current, which are inherently dependent on the precise position of the tip relative to the sample with the molecule, in addition to the instrumental function of the optical detection line. This will affect the intensity of emission lines as well as the background in any STML spectrum and consequently the contrast of the photon maps. Experimentally it was observed that the influence on the background intensity is partly mitigated on 3ML of NaCl in contrast to 2ML (as shown in our previous work),⁸⁸ likely due to a weaker direct tunneling of electrons between the tip and the metal below the NaCl. However in the measurements in this study, performed on 3ML of NaCl the background still plays a non-negligible role, which prevents correct interpretation of weaker excitonic contributions. Therefore we seek a robust normalization procedure that would reliably correct the spurious factors modulating a hyperspectral map.

We assume that the detected photons originate either from plasmons (excited by inelastic electrons directly transported across the tip-molecule-NaCl-metal system), or from the excitons (generated by charge injection into the molecule), as depicted in the scheme in the inset of the Fig.S5. Generation of such plasmonic and excitonic photons would be in a first approximation proportional to the intensity of the flow of charges (current) and the effectiveness of coupling to the nanocavity according to the actual tip-sample geometry. Detected spectra of the excitons and plasmons will finally be modulated by the spectral efficiency of the optical detection setup. We represent the net effect of all these factors by a

general modulation function $\Phi(r, E)$, which depends on the tip position r and energy E . The detected intensity of the photons can be then written as

$$I'(r, E) = \alpha \cdot I(r, E) \cdot \Phi(r, E) + \beta \cdot p(E) \cdot \Phi(r, E) \quad (3)$$

where the $I(r, E)$ is the excitonic emission spectrum, $p(E)$ the plasmonic response of the nanocavity material and α and β the respective exciton and plasmon yields. For simplicity we approximate $p(E)$ as a constant and substitute the term $\beta \cdot p(E) \cdot \Phi(r, E)$ for $\Phi'(r, E)$, which represents the effective measured plasmonic background. With this we obtain

$$I(r, E) \propto [I'(r, E) - \Phi'(r, E)] / \Phi'(r, E) \quad (4)$$

By estimating the $\Phi'(r, E)$ for each position r in the hyperspectral map, we can recover the excitonic spectra and normalize the photon maps for such r and E that yield a nonzero Φ' . For estimation of the plasmonic background, we exploit the continuous character of the plasmonic contribution as opposed to the excitonic signal, which consists of individual lines and can thus be relatively simply distinguished. An example of the photon map normalization is provided in the Fig.S6, which shows the perpendicular dimer before and after the process, including the intermediate step of the background subtraction. The comparison of the raw and processed photon maps to the theoretical prediction demonstrates the necessity of this step in suppressing the background signal of non-excitonic origin in order to yield photon maps suitable for comparison with the theoretical simulations. Nevertheless, a limitation of this approach arises from the assumption that we can determine the $\Phi'(r, E)$ in each location, which fails at very low tunneling currents, leading to a very low photon signal.

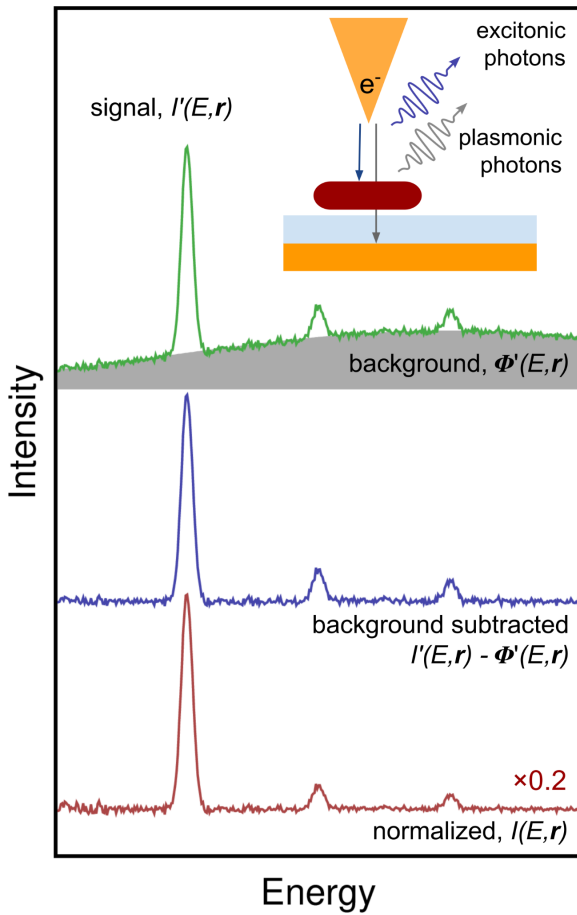


Figure S5. A visual explanation of the normalization procedure used for individual spectra comprising the hyperspectral maps. The detected signal $I'(r, E)$ is plotted by green color, the effective plasmonic background $\Phi'(r, E)$ by grey filled area. The excitonic part of the signal, plotted in blue, is divided by this general background to obtain the final normalized excitonic spectrum $I(r, E)$ (in red). The inset schematically depicts the basic concept of the electrons tunnelled directly between the tip and the metal substrate, inducing plasmons, or being captured by the molecule, and leading to exciton formation and radiative decay.

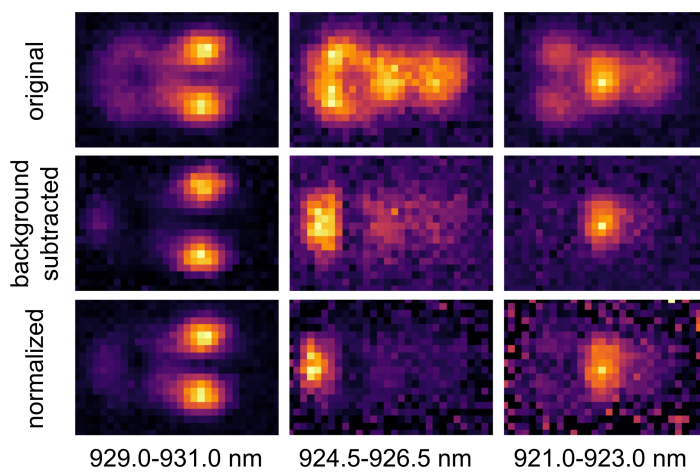


Figure S6. An example of the background subtraction and normalization of the hyperspectral maps taken at the perpendicular dimer.

DFT and TD-DFT calculations

All the quantum mechanical calculations were performed with the Gaussian16 package.^{S9} The ground state calculations were done with density functional method (DFT) employing wB97XD functional^{S10} and 6-31G* basis set. The presence of a more stable open shell solution was checked *via* the *stable* option and for open-shell systems UDFT has been used. The singlet excited state of neutral systems were computed with time-dependent (TD) DFT at the TD-wB97XD/6-31G* level of theory. For the triplet neutral and all the charged states, the Tamm-Dancoff approximation (TDA) has been used (TDA- ω B97X-D/6-31G*). The triplet to singlet excited states transitions were computed with the 50-50 option. PTCDA single molecule was optimized *in vacuo* in its neutral and anion ground states. The vertical excited states were assessed at the ground state equilibrium geometry and the emission properties were obtained by optimization of the corresponding excited state geometry (Table S1, Fig.S7). All aggregate model structures were built on the basis of the information provided by the analysis of the AFM images (Fig.S6), using the optimized PTCDA neutral geometry as basic units and neglecting the role of the substrate. For each aggregate several anionic states have been considered, by varying the number of total negative charges, and the most stable have been selected for further calculations (Table S2). In general, for each given total charge state, all relevant spin multiplicities have been computed with UDFT and provided near degenerate energies, due to a negligible spin interaction between the unpaired electrons. The total amount of charge localized on each molecular unit has been estimated based on Mulliken population analysis, by summing the partial charges on each atom within the molecule.^{S11} The aggregate exciton states (Tables S3-S8) were computed as vertical excitations, at a fixed geometry, on a selected spin state for each charge arrangement listed in Table S2 along with their oscillator strengths f , which characterize the linear absorption response of the system in the far field. The transition densities of selected states are used to simulate the corresponding photon maps. The transition densities were generated employing Multiwfn software (grid spacing 0.2 Bohr; plot with isosurface value set to 0.0001 e/Bohr³).^{S12}

Calculations on single molecule and aggregates

For the neutral molecule, the first excited state is represented by the HOMO→LUMO transition, with energy value 2.50 eV at the full TD-DFT level in excellent agreement with previously reported experimental data at 2.45 eV.^{S13} The anion displays two low-lying excited states close in energy, with emission at 1.62 and 1.80 eV, respectively. These values are slightly overestimated compared to the experimental emission (at 1.332 eV and 1.493 eV), consistently with that of the neutral excited state predicted at 2.79 eV when employing the TDA approximation. The corresponding transition dipole moments are oriented along the long and short molecular axes, respectively (see Fig.1 and Fig.S3). The calculation locates the triplet to singlet emission to lower energies, around 1.18 eV, also in agreement with the previous work.^{S13}

The aggregate exciton states computed with TD-DFT are linear combinations of single excitations involving orbitals delocalized on the whole system. In these PTCDA systems, the aggregate orbitals result from linear combinations of the molecular anionic orbitals localized

on each molecular unit. Thus, for each aggregate orbital, by a simple visual inspection, the dominant contributions to the combinations of molecular anionic orbitals can be identified. On the basis of this simple analysis it is possible to relate the calculated aggregate excitonic states (along with their corresponding transition densities) to the excitations localized on each molecular unit (longitudinal and transversal modes), whose interaction generates the excitonic states. The lookup tables and corresponding orbital energy schemes are summarized in Tables S3-S8 and Figs.S8-S13. We denote the molecular units in the aggregates with letters (*a-d*, see Table S2). The notation of the aggregate orbitals is chosen to reflect the base monomer orbital (H, L, H+1, L+1, *etc.*), the sign of the orbital linear combination (sign present in the upper index), and localization/delocalization on particular molecular units (a-d in upper indices). The spin branches are marked as α and β .

Charge state	transition	absorption E/eV (<i>f</i>)	absorption wavefunction ^c	emission E/eV (<i>f</i>)
neutral	$S_0 \leftrightarrow S_1^a$	2.91 (0.737)	0.98 (H \rightarrow L)	2.50 (0.716)
	$S_0 \leftrightarrow T_1^b$	1.77 (0)	0.90(H \rightarrow L)	1.18 (0)
anion ^b	$D_-^0 \leftrightarrow D_-^1$	1.84 (0.020)	0.66(H \rightarrow L) + 0.30 (L \rightarrow L+1)	1.62 (0.162)
	$D_-^0 \leftrightarrow D_-^2$	2.08 (0.072)	0.92 (L \rightarrow L+2)	1.80 (0.076)

^a Calculation with TD-wB97XD/6-31G*. ^b Calculation with TDA-wB97XD/6-31G*.

^c Molecular orbital naming refers to the order in the neutral molecule (see Fig. 1 main text).

Table S1. Computed emission energies (E), oscillator strengths (*f*) and wavefunctions composition (wf), including the most relevant coefficients and orbitals involved in the dominant excitations) for the isolated PTCDA molecule.

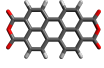
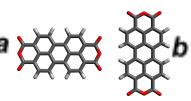
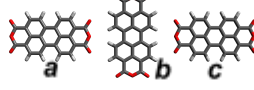
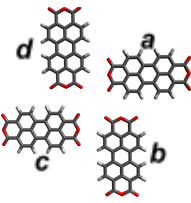
	charge (S) e ⁻	Relative Energy eV	charge localization				Scheme
			mol.a	mol.b	mol.c	mol.d	
monomer	-1 (1/2)	-2.65	-	-	-	-	
dimer parallel	-2 (1 or 0)	-3.63	-1.00	-1.00	-	-	
dimer perpendicular	-2 (1 or 0)	-3.64	-0.97	-1.03	-	-	
trimer	-2 (1 or 0)	-4.67	-0.97	-0.06	-0.97	-	
	-3 (3/2 or 1/2)	-4.09	-0.97	-1.06	-0.97	-	
tetramer	-3 (3/2)	-3.95	-0.75	-0.75	-0.75	-0.75	
	-3 (1/2)	-3.98	-0.50	-1.00	-0.50	-1.00	
	-2 (1 or 0)	-4.01	-0.01	-0.99	-0.01	-0.99	

Table S2. Total charge and spin of each system, absolute energy difference with respect to the neutral ground state, amount of charge localized on each molecule of the aggregate (labeled according to the scheme in the last column), computed at the wB97XD/6-31G* level of theory.

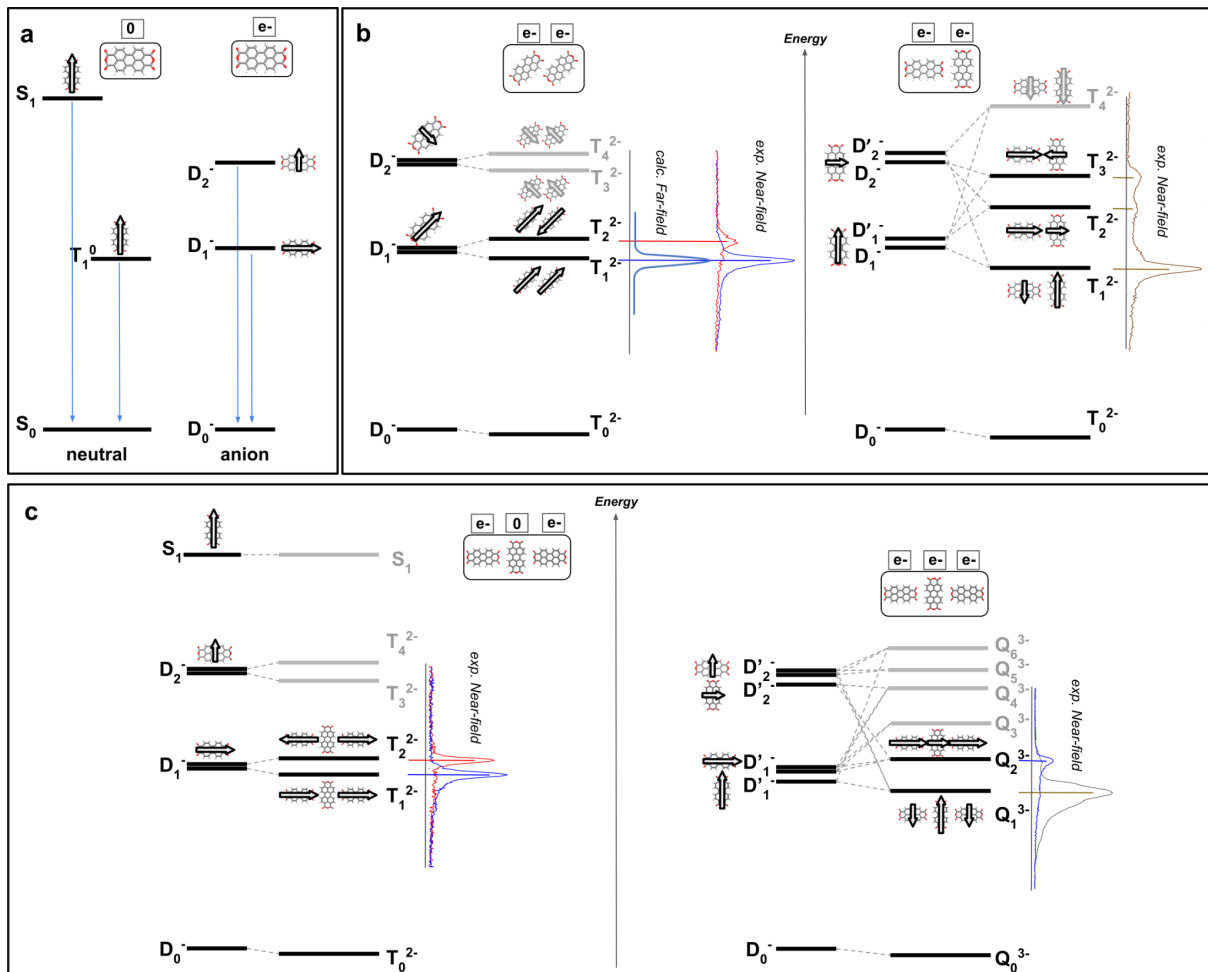


Figure S7. (a) Energy level scheme of the PTCDA neutral and anion monomer excited states (see Table S1). (b) Energy level scheme of PTCDA dimer excitonic states (parallel dimer on the left and perpendicular dimer on the right, see also Tables S3 and S4): their relation with respect to the monomer states in terms of energies and wavefunctions (represented by the transition dipole moment arrow) and relation to the experimental spectra (Figs. 1-3). For the parallel dimer (left), the comparison with the computed *far-field* spectrum is highlighted. (c) Energy level scheme of PTCDA trimer excitonic states, for total charge -2 (left) and -3 (right) (see Tables S3 and S4) and their relation with the composing monomer states and with the experimental spectra (Figs. 1-3).

dimer parallel S = 1	E/eV (<i>f</i>)	wf.^a
T ₁ ²⁻ (Bu)	1.852 (0.296)	0.39 L _{<i>a</i>} ⁺ → L+1 _{<i>a</i>} ⁺ 0.35 L _{<i>a</i>} ⁻ → L+1 _{<i>a</i>} ⁻ 0.11 H _{<i>β</i>} → L _{<i>β</i>} 0.11 H _{<i>β</i>} ⁺ → L _{<i>β</i>} 0.01 L _{<i>a</i>} ⁻ → L+2 _{<i>a</i>} ⁻
T ₂ ²⁻ (Ag)	1.857 (0)	0.36 L _{<i>a</i>} ⁺ → L+1 _{<i>a</i>} ⁻ 0.34 L _{<i>a</i>} ⁻ → L+1 _{<i>a</i>} ⁺ 0.11 H _{<i>β</i>} ⁺ → L _{<i>β</i>} 0.11 H _{<i>β</i>} → L _{<i>β</i>} ⁺ 0.03 L _{<i>a</i>} ⁻ → L+2 _{<i>a</i>} ⁺ 0.01 L _{<i>a</i>} ⁺ → L+2 _{<i>a</i>} ⁻
T ₃ ²⁻ (Bu)	1.906 (0.165)	0.44 L _{<i>a</i>} ⁻ → L+2 _{<i>a</i>} ⁻ 0.47 L _{<i>a</i>} ⁺ → L+2 _{<i>a</i>} ⁺ 0.01 L _{<i>a</i>} ⁻ → L+1 _{<i>a</i>} ⁻
T ₄ ²⁻ (Ag)	1.923 (0)	0.43 L _{<i>a</i>} ⁻ → L+2 _{<i>a</i>} ⁺ 0.43 L _{<i>a</i>} ⁺ → L+2 _{<i>a</i>} ⁻ 0.01 L _{<i>a</i>} ⁻ → L+1 _{<i>a</i>} ⁺

^a For the orbitals notation, refer to Fig. S8.

Table S3. Vertical excited states of the parallel dimer (total charge -2, triplet spin state): excitation energies (E), oscillator strengths (*f*) and wavefunction composition (wf) including coefficients and aggregate orbitals involved in the dominant excitations (coefficients ≥ 0.01).

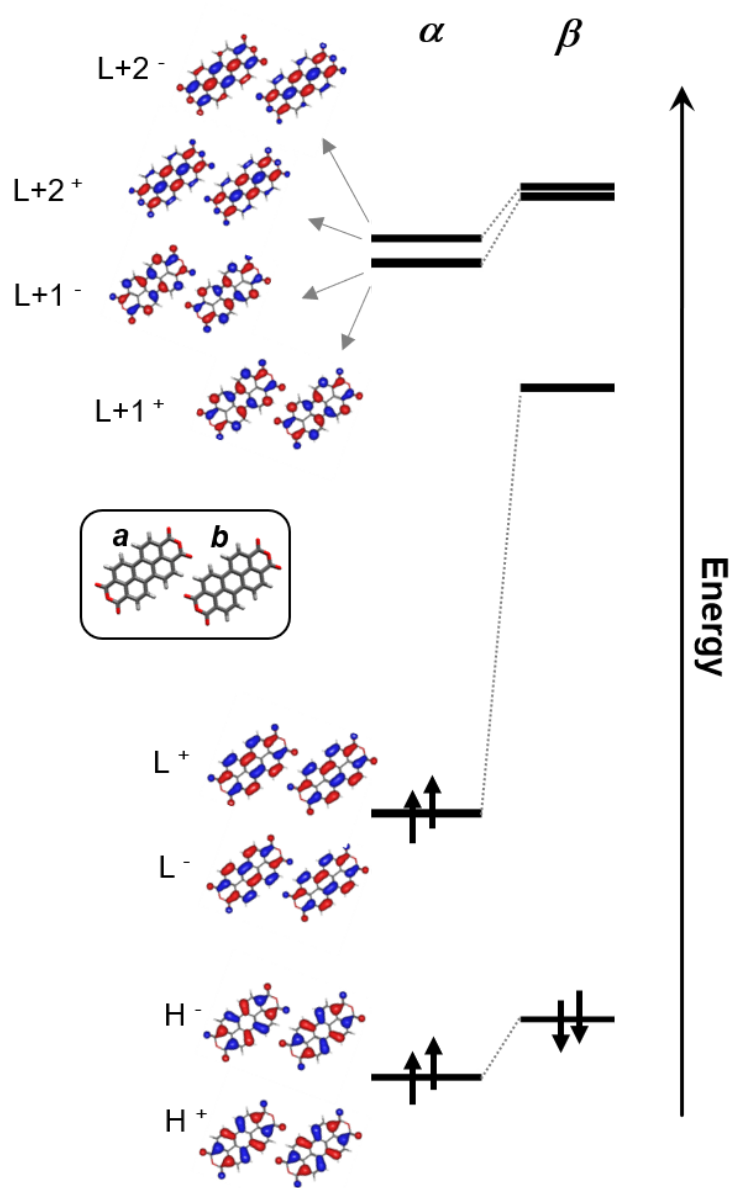


Figure S8. Scheme of the ground state aggregate orbitals involved in the relevant vertical excited states of the parallel dimer (total charge -2, triplet spin state).

dimer perpendicular S = 1	E/eV (<i>f</i>)	wf ^a
T ₁ ²⁻ (B2)	1.852 (0.108)	0.73 L ^a _α → L+1 ^a _α 0.22 H ^a _β → L ^a _β 0.01 L ^b _α → L+2 ^b _α
T ₂ ²⁻ (A1)	1.872 (0.189)	0.70 L ^b _α → L+1 ^b _α 0.22 H ^b _β → L ^b _β 0.05 L ^a _α → L+2 ^a _α
T ₃ ²⁻ (A1)	1.915 (0.052)	0.88 L ^a _α → L+2 ^a _α 0.03 L ^b _α → L+1 ^b _α 0.02 L ^b _β → L+2 ^b _β
T ₄ ²⁻ (B2)	1.920 (0.081)	0.91 L ^b _α → L+2 ^b _α

^a For the orbitals notation, refer to Fig.S9.

Table S4. Vertical excited states of the perpendicular dimer (total charge -2, triplet spin state): excitation energies (E), oscillator strengths (*f*) and wavefunction composition (wf) including coefficients and aggregate orbitals involved in the dominant excitations (coefficients ≥ 0.01).

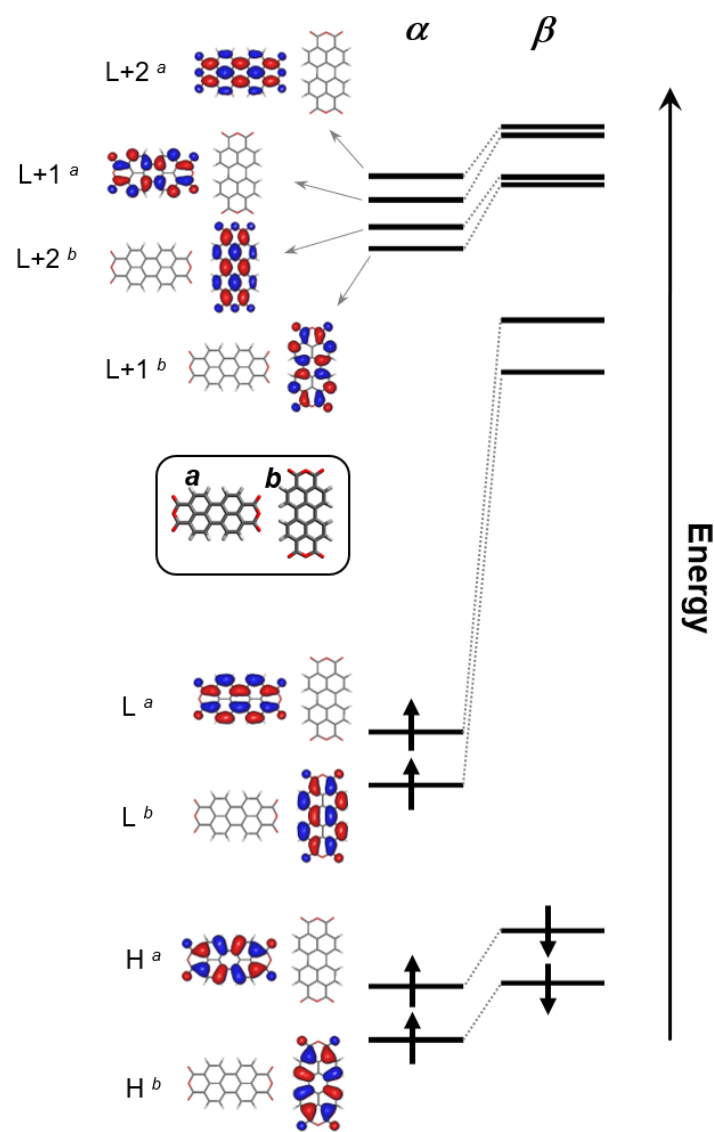


Figure S9. Scheme of the ground state aggregate orbitals involved in the relevant vertical excited states of the perpendicular dimer (total charge -2, triplet spin state).

trimer ^a S = 1	E/eV (<i>f</i>)	wf. ^b
T ₁ ²⁻ (B1u)	1.863 (0.309)	0.37 L _{α} ⁻ \rightarrow L+L _{α} ⁻ 0.37 L _{α} ⁺ \rightarrow L+L _{α} ⁺ 0.11 H _{β} ⁺ \rightarrow L _{β} ⁺ 0.11 H _{β} ⁻ \rightarrow L _{β} ⁻
T ₂ ²⁻ (Ag)	1.878 (0)	0.36 L _{α} ⁻ \rightarrow L+L _{α} ⁺ 0.36 L _{α} ⁺ \rightarrow L+L _{α} ⁻ 0.12 H _{β} ⁺ \rightarrow L _{β} ⁻ 0.12 H _{β} ⁻ \rightarrow L _{β} ⁺
T ₃ ²⁻ (B3g)	1.916 (0)	0.46 L _{α} ⁻ \rightarrow L+L _{α} ⁺ 0.46 L _{α} ⁺ \rightarrow L+L _{α} ⁻
T ₄ ²⁻ (B2u)	1.917 (0.130)	0.46 L _{α} ⁻ \rightarrow L+L _{α} ⁺ 0.46 L _{α} ⁺ \rightarrow L+L _{α} ⁻

^a The excited state ordering from calculations is 4-7 (the lower states were discarded).

^b For the orbitals notation, refer to Fig. S10.

Table S5. Vertical excited states of the trimer (total charge -2, triplet spin state): excitation energies (E), oscillator strengths (*f*) and wavefunction composition (wf) including coefficients and aggregate orbitals involved in the dominant excitations (coefficients ≥ 0.01).

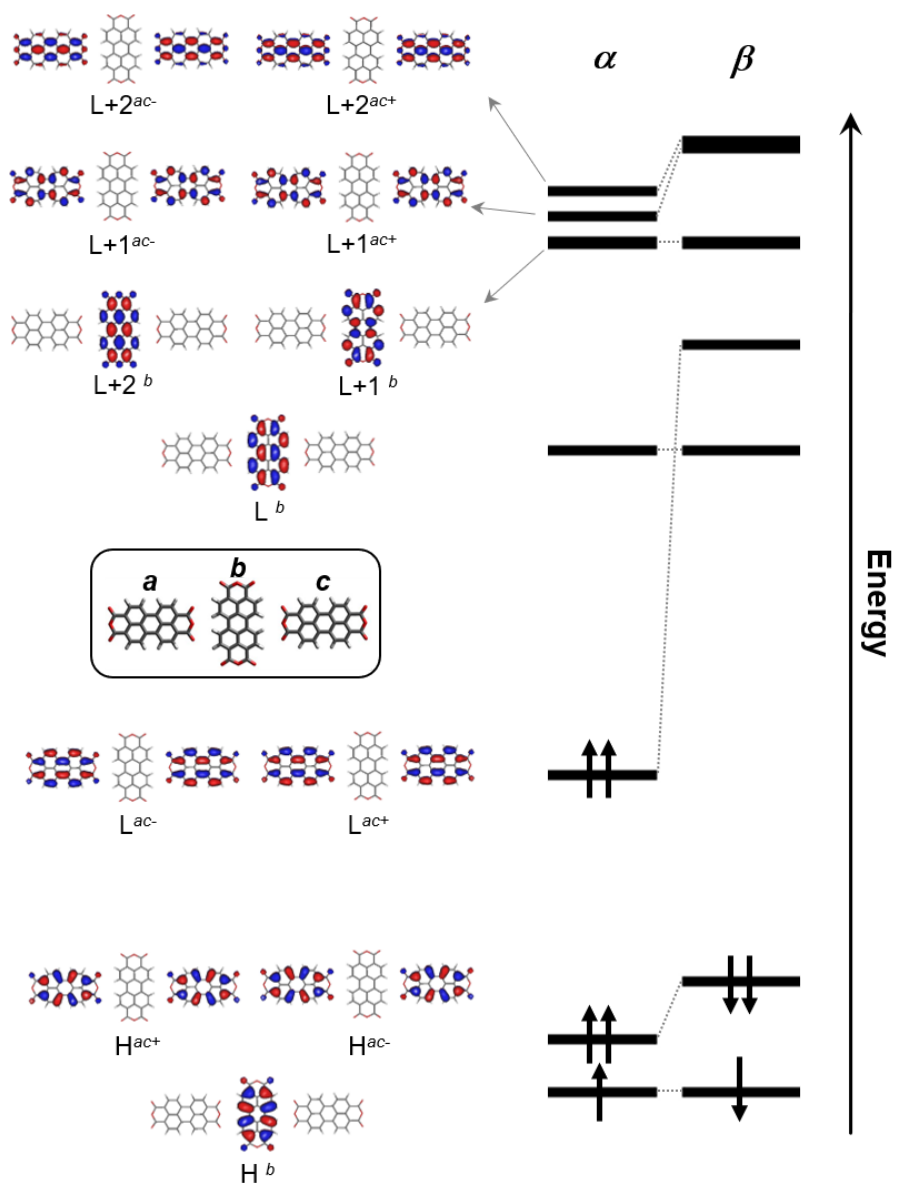


Figure S10. Scheme of the ground state aggregate orbitals involved in the relevant vertical excited states of the trimer (total charge -2, triplet spin state).

trimer S = 3/2	E/eV (f)	wf.^a
$Q_1^{3^-}$ (B2u)	1.841(0.094)	$0.74 L_a^b \rightarrow L+1_a^b$
		$0.21 H_\beta^b \rightarrow L_\beta^b$
$Q_2^{3^-}$ (B1u)	1.869(0.413)	$0.35 L_a^b \rightarrow L+2_a^b$
		$0.24 L_{\alpha}^{ac^-} \rightarrow L+1_{\alpha}^{ac^-}$
		$0.24 L_{\alpha}^{ac^+} \rightarrow L+1_{\alpha}^{ac^+}$
		$0.06 H_\beta^{ac^+} \rightarrow L_\beta^{ac^+}$
		$0.06 H_\beta^{ac^-} \rightarrow L_\beta^{ac^-}$
$Q_3^{3^-}$ (Ag)	1.884(0)	$0.36 L_{\alpha}^{ac^-} \rightarrow L+1_{\alpha}^{ac^+}$
		$0.36 L_{\alpha}^{ac^+} \rightarrow L+1_{\alpha}^{ac^-}$
		$0.12 H_\beta^{ac^+} \rightarrow L_\beta^{ac^-}$
		$0.12 H_\beta^{ac^-} \rightarrow L_\beta^{ac^+}$
$Q_4^{3^-}$ (B1u)	1.897(0.001)	$0.58 L_a^b \rightarrow L+2_a^b$
		$0.13 L_{\alpha}^{ac^-} \rightarrow L+1_{\alpha}^{ac^-}$
		$0.13 L_{\alpha}^{ac^+} \rightarrow L+1_{\alpha}^{ac^+}$
		$0.06 H_\beta^{ac^+} \rightarrow L_\beta^{ac^+}$
		$0.06 H_\beta^{ac^-} \rightarrow L_\beta^{ac^-}$
$Q_5^{3^-}$ (B3g)	1.917(0)	$0.46 L_{\alpha}^{ac^-} \rightarrow L+2_{\alpha}^{ac^+}$
		$0.46 L_{\alpha}^{ac^+} \rightarrow L+2_{\alpha}^{ac^-}$
$Q_6^{3^-}$ (B2u)	1.919(0.157)	$0.45 L_{\alpha}^{ac^-} \rightarrow L+2_{\alpha}^{ac^-}$
		$0.45 L_{\alpha}^{ac^+} \rightarrow L+2_{\alpha}^{ac^+}$
		$0.01 L_a^b \rightarrow L+1_a^b$

^a for the orbitals notation, refer to Fig. S11.

Table S6. Vertical excited states of the trimer (total charge -3, quartet spin state): excitation energies (E), oscillator strengths (f) and wavefunction composition (wf) including coefficients and aggregate orbitals involved in the dominant excitations (coefficients ≥ 0.01).

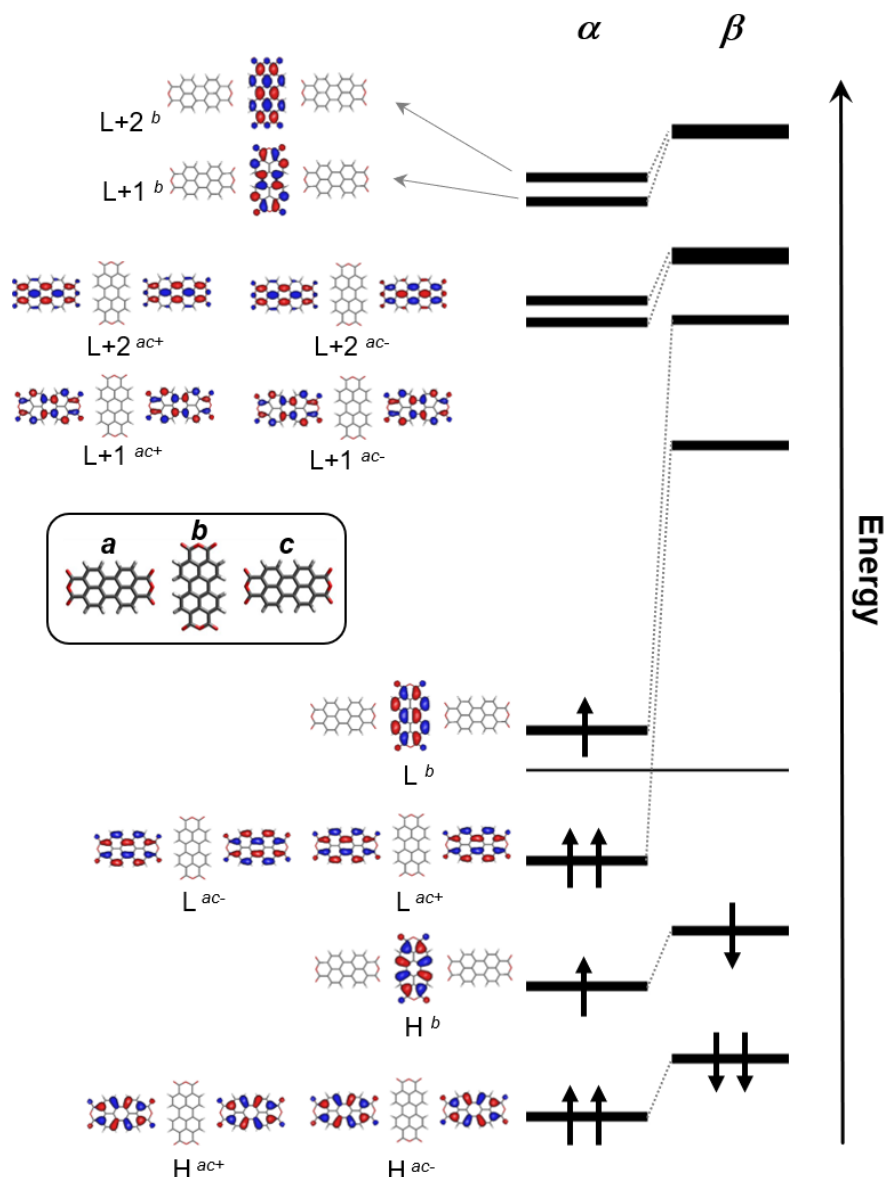


Figure S11. Scheme of the ground state aggregate orbitals involved in the relevant vertical excited states of the trimer (total charge -3, quartet spin state).

Tetramer ^a S = 3/2	E/eV (f)	wf. ^b
Q ₁ ³⁻ (Bg)	1.824(0)	0.20 L ^{t-} _α → L ^{t+} _α 0.20 L ^{ac-} _α → L+1 ^{ac-} _α 0.20 L ^{bd-} _α → L+1 ^{bd-} _α 0.08 H ^{t-} _α → L ^{t+} _α 0.07 H ^{t+} _β → L ^{t-} _β 0.07 H ^{t-} _β → L ^{t+} _β 0.06 H ^{ac-} _β → L ^{ac-} _β 0.06 H ^{bd-} _β → L ^{bd-} _β
Q ₂ ³⁻ (Eu)	1.826(0.185)	0.17 L ^{bd-} _α → L+1 ^{t+} _α 0.16 L ^{t-} _α → L+1 ^{bd-} _α 0.15 L ^{bd-} _α → L+1 ^{t-} _α 0.06 H ^{bd-} _β → L ^{t-} _β 0.06 H ^{ac-} _α → L ^{t+} _α 0.06 H ^{t+} _β → L ^{bd+} _β 0.05 H ^{t+} _β → L ^{bd-} _β 0.05 L ^{ac-} _α → L+1 ^{t-} _α
Q ₃ ³⁻ (Eu)	1.826(0.185)	0.17 L ^{ac-} _α → L+1 ^{t+} _α 0.16 L ^{t-} _α → L+1 ^{ac+} _α 0.15 L ^{ac-} _α → L+1 ^{t-} _α 0.06 H ^{ac-} _β → L ^{t-} _β 0.06 H ^{bd-} _α → L ^{t+} _α 0.06 H ^{t-} _β → L ^{ac-} _β 0.05 H ^{t+} _β → L ^{ac-} _β 0.05 L ^{bd-} _α → L+1 ^{t-} _α
Q ₄ ³⁻	1.828(0)	0.19 L ^{ac-} _α → L+1 ^{ac+} _α 0.19 L ^{bd-} _α → L+1 ^{bd-} _α 0.19 L ^{t-} _α → L+1 ^{t-} _α 0.07 H ^{t+} _α → L ^{t+} _α 0.07 H ^{t-} _β → L ^{t-} _β 0.07 H ^{t+} _β → L ^{t+} _β 0.07 H ^{ac-} _β → L ^{ac-} _β 0.07 H ^{bd-} _β → L ^{bd-} _β

^aThe excited state ordering from calculations is 4-7 (lower states were discarded).

^b For the orbitals notation refer to Fig.S12. The notation “ac⁺bd⁺” has been shortened to “t”.

Table S7. Vertical excited states of the tetramer (total charge -3, quartet spin state): excitation energies (E), oscillator strengths (f) and wavefunction composition (wf) including coefficients and aggregate orbitals involved in the dominant excitations (coefficients ≥ 0.05).

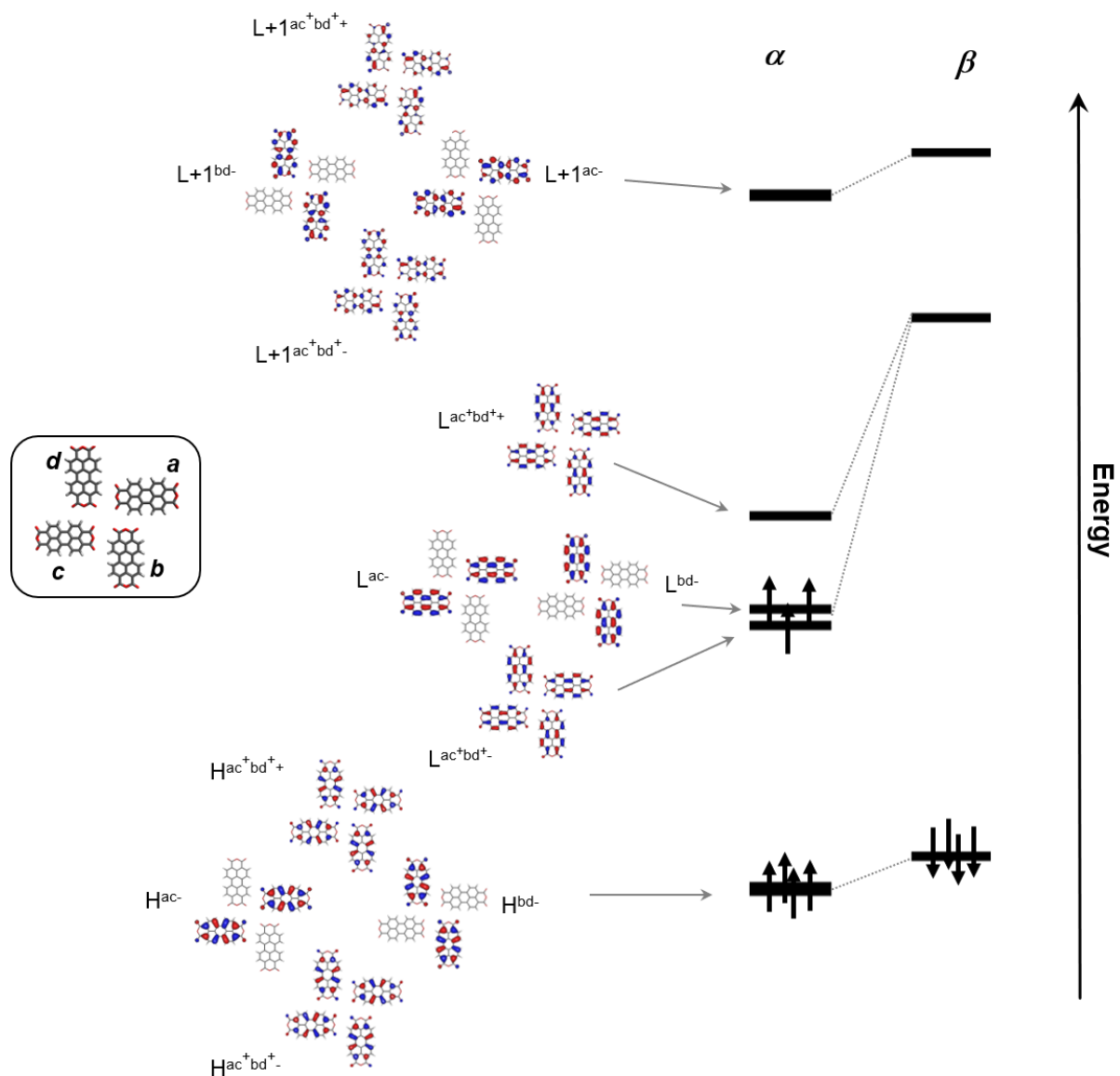


Figure S12. Scheme of the ground state aggregate orbitals involved in the relevant vertical excited states of the tetramer (total charge -3, quartet spin state).

Tetramer ^a S = 1	E/eV (<i>f</i>)	wf. ^b
T_1^{-2} (Bg)	1.845 (0.283)	
		$0.37 L_a^{ac-} \rightarrow L+1_a^{ac-}$
		$0.37 L_a^{ac+} \rightarrow L+1_a^{ac+}$
		$0.09 H_\beta^{ac+} \rightarrow L_\beta^{ac+}$
		$0.09 H_\beta^{ac-} \rightarrow L_\beta^{ac-}$
		$0.02 L_a^{ac-} \rightarrow L+2_a^{ac-}$
		$0.02 L_a^{ac+} \rightarrow L+2_a^{ac+}$

^aThe excited state ordering number from calculations is 7 (the lower states were discarded).

^bFor the orbitals notation, refer to Fig.S13.

Table S8. Vertical excited states of the tetramer (total charge -2, triplet spin state): excitation energies (E), oscillator strengths (*f*) and wavefunction composition (wf) including coefficients and aggregate orbitals involved in the dominant excitations (coefficients ≥ 0.05).

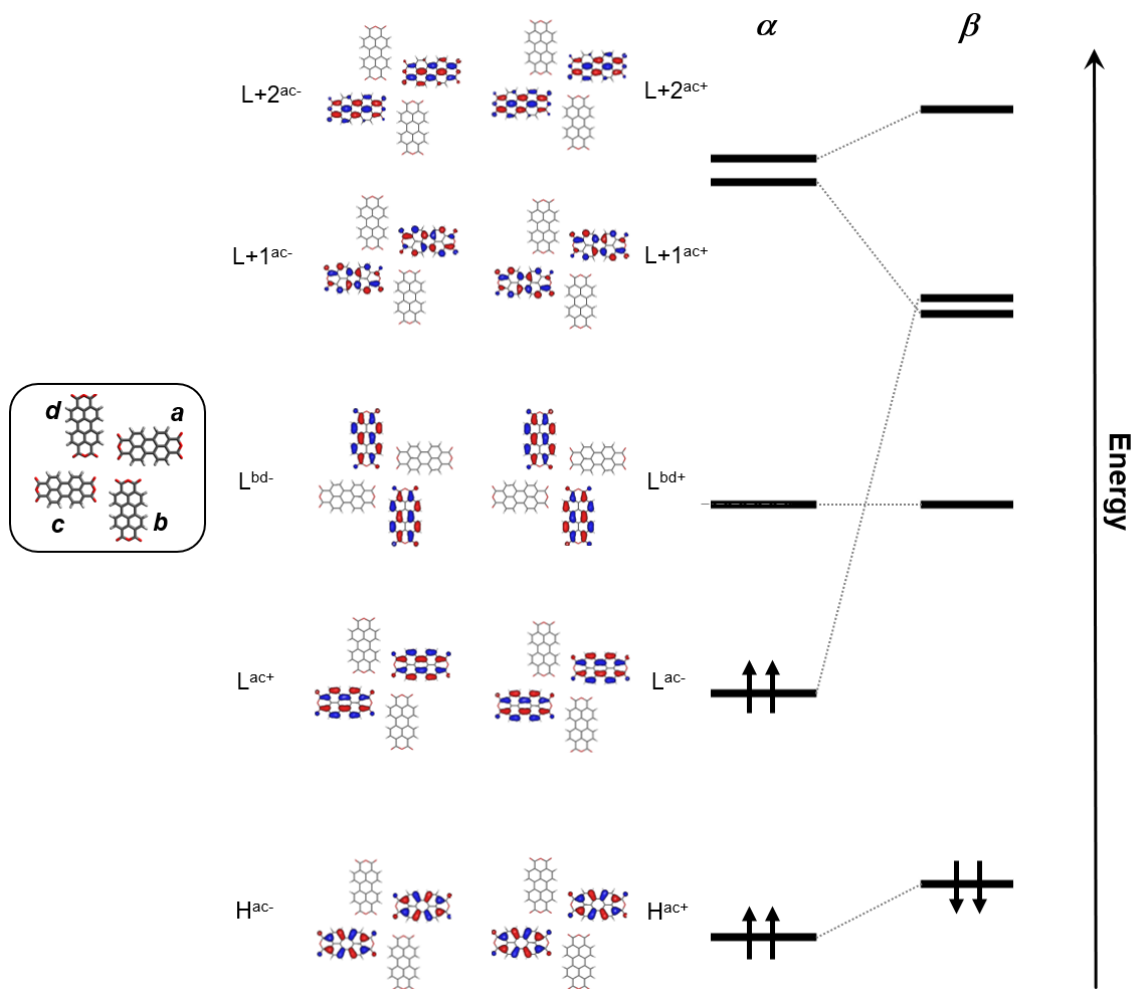


Figure S13. Scheme of the ground state aggregate orbitals involved in the relevant vertical excited states of the tetramer (total charge -2, triplet spin state).

Supporting Information references

- S1. Hapala, P. *ProbeParticleModel* <https://github.com/ProkopHapala/ProbeParticleModel>; GitHub repository, **2014**.
- S2. Neuman, T.; Esteban, R.; Casanova, D.; García-Vidal, F. J.; Aizpurua, J. Coupling of Molecular Emitters and Plasmonic Cavities beyond the Point-Dipole Approximation. *Nano Lett.* **2018**, 18, 2358–2364.
- S3. Doležal, J.; Canola, S.; Merino, P.; Švec, M. Exciton-Trion Conversion Dynamics in a Single Molecule. *ACS Nano* **2021**, 15, 7694–7699.
- S4. Doležal, J.; Merino, P.; Švec, M. Constant Amplitude Driving of a Radio Frequency Excited Plasmonic Tunnel Junction. *Appl. Phys. Lett.* **2021**, 118, 193301.
- S5. Cochrane, K. A.; Schiffrin, A.; Roussy, T. S.; Capsoni, M.; Burke, S. A. Pronounced Polarization-Induced Energy Level Shifts at Boundaries of Organic Semiconductor Nanostructures. *Nat. Commun.* **2015**, 6, 8312.
- S6. Burke, S.A.; Ji, W.; Mativetsky, J. M.; Topple, J.M.; Fostner, S.; Gao, H. J.; Guo, H.; Grütter, P. Strain Induced Dewetting of a Molecular System: Bimodal Growth of PTCDA on NaCl. *Phys. Rev. Lett.* **2008**, 100, 186104.
- S7. Scheuerer, P.; Patera, L. L.; Repp, J. Manipulating and Probing the Distribution of Excess Electrons in an Electrically Isolated Self-Assembled Molecular Structure. *Nano Lett.* **2020**, 20, 1839–1845.
- S8. Doležal, J.; Mutombo, P.; Nachtigallová, D.; Jelínek, P.; Merino, P.; Švec, M. Mechano-Optical Switching of a Single Molecule with Doublet Emission. *ACS Nano* **2020**, 14, 8931–8938.
- S9. Frisch, M. J.; Trucks, G. W.; Schlegel, H. B.; Scuseria, G. E.; Robb, M. A.; Cheeseman, J. R.; Scalmani, G.; Barone, V.; Petersson, G. A.; Nakatsuji, H.; Li, X.; Caricato, M.; Marenich, A. V.; Bloino, J.; Janesko, B. G.; Gomperts, R.; Mennucci, B.; Hratchian, H. P.; Ortiz, J. V.; Izmaylov, A. F.; Sonnenberg, J. L. *et al.* *Gaussian 16*, Revision A.03; Gaussian, Inc.: Wallingford CT, **2016**.
- S10. Chai, J.-D.; Head-Gordon, M. Long-Range Corrected Hybrid Density Functionals with Damped Atom-Atom Dispersion Corrections. *Phys. Chem. Chem. Phys.* **2008**, 10, 6615–6620.
- S11. Mulliken, R. S. Electronic Population Analysis on LCAO–MO Molecular Wave Functions. I. *J. Chem. Phys.* **1955**, 23, 1833–1840.
- S12. Lu, T.; Chen, F. Multiwfn: A Multifunctional Wavefunction Analyzer. *J. Comput. Chem.* **2012**, 33, 580–592.
- S13. Kimura, K.; Miwa, K.; Imada, H.; Imai-Imada, M.; Kawahara, S.; Takeya, J.; Kawai, M.; Galperin, M.; Kim, Y. Selective Triplet Exciton Formation in a Single Molecule. *Nature* **2019**, 570, 210–213.